# Orbital-selective two-dimensional superconductivity in 2H-$NbS_2$

Xiangyu Bi,[1] Zeya Li,[1] Junwei Huang,[1] Feng Qin,[2,1,*] Caorong Zhang,[1] Zian Xu,[3] Ling Zhou,[1] Ming Tang,[1] Caiyu Qiu,[1] Peizhe Tang,[3,4] Toshiya Ideue,[2] Tsutomu Nojima,[5] Yoshihiro Iwasa,[2] and Hongtao Yuan[1,†]

[1]*College of Engineering and Applied Sciences, National Laboratory of Solid State Microstructures and Jiangsu Key Laboratory of Artificial Functional Materials, Nanjing University, Nanjing 210000, China*

[2]*Quantum Phase Electronic Center and Department of Applied Physics, The University of Tokyo, Tokyo 113-8656, Japan*

[3]*School of Materials Science and Engineering, Beihang University, Beijing 100191, China*

[4]*Max Planck Institute for the Structure and Dynamics of Matter, Center for Free Electron Laser Science, Hamburg 22761, Germany*

[5]*Institute for Materials Research, Tohoku University, Sendai 980-8577, Japan*

(Received 10 October 2021; accepted 9 February 2022; published 8 March 2022)

Orbital-selective superconductivity is crucial for understanding the pairing mechanism for multiband superconductors. Atomic *d* orbitals with anisotropic spatial extension can directly determine the energy dispersion of subbands with two-dimensional (2D) or three-dimensional (3D) nature in band structure. Theoretically, owing to the coexistence of these 2D and 3D subbands, the orbital-selective superconductivity can exhibit band-dependent dimensionality in multiband superconductors. However, to experimentally confirm this orbital-selective 2D superconductivity remains challenging and elusive. Herein, based on angle-dependent upper critical magnetic field on 2H-$NbS_2$ flakes, we observe a cusp peak associated with a 2D superconducting subband from the $d_{xy}$ and $d_{x^2-y^2}$ orbitals of Nb atoms, and a round peak related to a 3D subband, directly confirming the existence of intrinsic 2D superconductivity in 2H-$NbS_2$ thick flake and its orbital-selective superconducting nature. The 2D superconductivity remains robust under large electric current or high pressure. Such observations shed light on the orbital-selective pairing mechanism and resulting band-dependent dimensionality for multiband superconductors.

DOI: 10.1103/PhysRevResearch.4.013188

## I. INTRODUCTION

Multiband superconductors, well described by Ginzburg-Landau theory [1,2], serve as a crucial platform for understanding orbital-selective pairing mechanisms and emergent superconducting phenomena. Examples of multiple superconducting gaps have been demonstrated in FeSe, $MgB_2$, and $NbSe_2$ [3–7], where the subbands with specific orbital components crossing Fermi energy can form orbital-selective superconducting gaps. Unlike the single-band superconductors where the ground state of a specific energy band is solely a superconducting state by excluding other competing orderings such as charge density wave [8] or antiferromagnetism [9], the multiband superconductors allow the coexistence of the above-mentioned electronic orderings by accommodating the competing states separately in different subbands [10–13]. Specifically, emergent superconducting phenomena, such as multiple superconducting gaps and the underlying orbital-selective pairing mechanism, directly originate from the specific orbital components of the subbands. The dimensional nature of multiband superconductivity [14–17] can thus be directly determined by the energy dispersion of each subband whose dimensionality comes from the spatial distribution of orbitals and their overlapping. Therefore, two-dimensional (2D) superconductivity should be observable in multiband superconductors as a direct result of the orbital-selective pairing mechanism within the 2D-like subband (associated with the 2D superconducting gap), irrespective of the sample dimension. However, an experimental confirmation of such an orbital-selective 2D superconductivity in multiband superconductors remains challenging.

In this paper, combining the measurements of angle-dependent upper critical magnetic field $H_C(\theta)$ with the analysis of the Ginzburg-Landau theory, we demonstrate an orbital-selective 2D superconductivity and its coexistence with three-dimensional (3D) superconductivity in thick flakes of the multiband 2H-$NbS_2$ superconductor. We observe the round peak in the $H_C(\theta)$ curve with the $\theta$ far away from 90° ($\theta$ measured from the normal vector of the sample plane), well fitted by a 3D Ginzburg-Landau equation, indicating the existence of the expected 3D superconductivity in flakes with a thickness of 35–45 nm. Surprisingly, the $H_C(\theta)$ curve near $\theta = 90°$ displays a clear cusp peak well explained by the Tinkham equation, providing direct evidence of a 2D component in such a superconducting system. Our observations indicate that these 3D and 2D superconducting components directly originate from an orbital-selective pairing mechanism

*qinfeng@mp.t.u-tokyo.ac.jp
†htyuan@nju.edu.cn

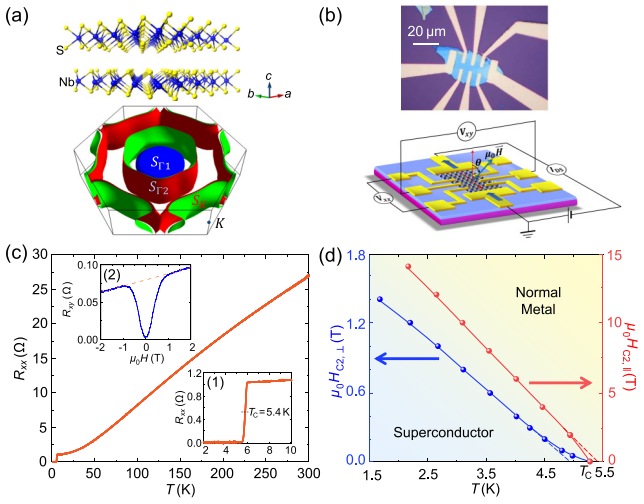


FIG. 1. Fundamental physical properties of a typical superconducting 2H-$NbS_2$ flake. (a) Upper panel: Ball-and-stick crystal structure of 2H-$NbS_2$, with blue and yellow balls representing Nb and S atoms, respectively. Lower panel: The Brillouin zone and calculated Fermi surface of 2H-$NbS_2$. $S_{\Gamma 1}$ and $S_{\Gamma 2}$ represent Fermi surface sheets around the Γ point and $S_K$ represents the Fermi surface sheet around the $K$ point. (b) Schematic illustration and optical image of the device. Samples with thickness of around 45 nm are intentionally chosen. (c) Temperature dependence of four-terminal resistance $R_{xx}$. The resistance of metallic 2H-$NbS_2$ is generally linear to the temperature $T$ above 50 K, majorly dominated by electron-phonon scattering. Inset (1) is the partial enlargement near $T_C = 5.4$ K (defined by 50% $R_N$), and inset (2) is the Hall resistance $R_{xy}$ measured at 4 K. The total carrier density $n \approx 1.78 \times 10^{22}$ cm$^{-3}$ is obtained by linear fitting (red dashed line) of the $R_{xy}$-$\mu_0 H$ relation at high fields. (d) the $H_C$-$T$ phase diagram. $H_C$ is also defined by 50% $R_N$. Note that, near $T_C$, the $H_C$-$T$ relations significantly deviate from the linear behavior (see red and blue dashed lines).

in specific subbands with different orbital components. Such findings provide an opportunity to achieve band-dependent dimensionality of superconductivity, and to understand the orbital-selective pairing mechanism in multiband van der Waals superconductors.

## II. RESULTS

We choose 2H-$NbS_2$ as our target material because of the following three reasons: Firstly, 2H-$NbS_2$ has a van der Waals layered structure with anisotropic dispersion in band structures, and shows multiband superconductivity behavior [16,18–21]. At the Fermi level, two electronic states centered at the Γ point in the Brillouin zone show 3D behavior while the third state centered at the $K$ point shows 2D-like behavior [Fig. 1(a)]. Secondly, as confirmed by theoretical calculations on the orbital components and the electron pairing of the subbands [16], the interband coupling between subbands centered at the $K$ and Γ points of 2H-$NbS_2$ is weak due to the orthogonality of atomic orbitals, making multiband 2H-$NbS_2$ an extraordinary platform to study the orbital-selective superconducting feature originating from specific subbands [5]. Thirdly, in contrast to its counterparts such as multiband superconductors 2H-$TaSe_2$ and 2H-$NbSe_2$ whose superconducting states are mixed with the charge density wave states [17,22,23], pristine 2H-$NbS_2$ has no charge density wave state in the phase diagram [18,24] and can serve as a clean system to investigate the orbital-selective multiband superconductivity.

Figure 1(b) shows a schematic diagram and an optical photograph of a typical Hall-bar device of 2H-$NbS_2$, and Fig. 1(c) presents the corresponding temperature-dependent four-terminal resistance $R_{xx}$. Inset (1) is the partial enlargement of the temperature near the superconducting transition region, and the superconducting critical temperature $T_C = 5.4$ K is defined by 50% $R_N$, where $R_N$ is defined as the normal state resistance $R_{xx}(6.5\ \text{K})$. The steep decrease of resistance with temperature provides evidence of a 3D superconductor. Distinct from its counterpart 2H-$NbSe_2$, the smooth shape without resistance bump in the $R_{xx}$-$T$ curve above $T_C$ implies the absence of a charge density wave state [22–24].

In order to understand the highly anisotropic behavior of the upper critical magnetic field of the superconductivity, the $R_{xx}$-$T$ curves under the out-of-plane and in-plane magnetic fields are investigated. The corresponding temperature-dependent phase diagram for the out-of-plane ($H_{C2,\perp}$) and in-plane ($H_{C2,\parallel}$) upper critical magnetic fields (defined by the value of magnetic field when $R_{xx} = 50\%\ R_N$) is shown in Fig. 1(d), and two important things need to be addressed here: Firstly, when the temperature is below 4.5 K, the linear $H_{C2}$-$T$ relations $H_{C2} \propto (1 - T/T_C)$ for both $H_{C2,\parallel}$ and $H_{C2,\perp}$ can be well explained by the conventional anisotropic 3D Ginzburg-Landau theory, in sharp contrast with those 2D-like superconducting systems [6] satisfying $H_{C2} \propto (1 - T/T_C)^{1/2}$. At the temperatures above 4.5 K, the $H_{C2}$-$T$ relations for both $H_{C2,\perp}$ and $H_{C2,\parallel}$ slightly deviate from the linear extrapolations, especially for the $T$ close to $T_C$. The $H_{C2,\perp}$ is obviously larger than the extrapolated value and displays a concave shape, which can be explained by the multiband superconducting nature of 2H-$NbS_2$. In contrast, the $H_{C2,\parallel}$ is slightly smaller than the linear extrapolation, and such convex shape of the $H_{C2,\parallel}$ implies that 2D superconductivity might also exist in superconducting thick 2H-$NbS_2$ flakes (more details will be discussed later). Secondly, the zero-temperature upper critical fields are estimated to be $\mu_0 H_{C2,\perp}(0\ \text{K}) = \Phi_0/2\pi\xi_{ab}^2 = 2.24$ T and $\mu_0 H_{C2,\parallel}(0\ \text{K}) = \Phi_0/2\pi\xi_{ab}\xi_c = 25.4$ T by extrapolating the linear relation to 0 K, where $\Phi_0 \approx 2.07 \times 10^{-15}$ Wb is the magnetic flux quantum, $\xi_{ab}$ is the in-plane coherence length, and $\xi_c$ is the out-of-plane coherence length. Therefore, the $\xi_{ab}(0\ \text{K})$ is about 12.1 nm, and the $\xi_c(0\ \text{K})$ is about 1.07 nm. The anisotropy index, $\xi_{ab}/\xi_c = 11.3$, is much larger than that value of approximately 3 in the 2H-$NbSe_2$ crystal [25], indicating that 2H-$NbS_2$ has even stronger anisotropy.

To accurately verify the dimensionality of superconductivity associated with each subband, two experimental criteria are generally used: (1) By comparing the out-of-plane coherence length $\xi_c$ to the superconducting thickness $d$, the superconducting system is considered to be 2D-like if $\xi_c \gg d$, and vice versa. Note that, compared to the typical thickness $d$ (35–45 nm; see Supplemental Material Fig. S1 [26]) of our measured samples, the out-of-plane coherence length $\xi_c$ is much smaller ($\xi_c \ll d$). While the $\xi_c$ value based on the formula derived from single-band superconductors is frequently

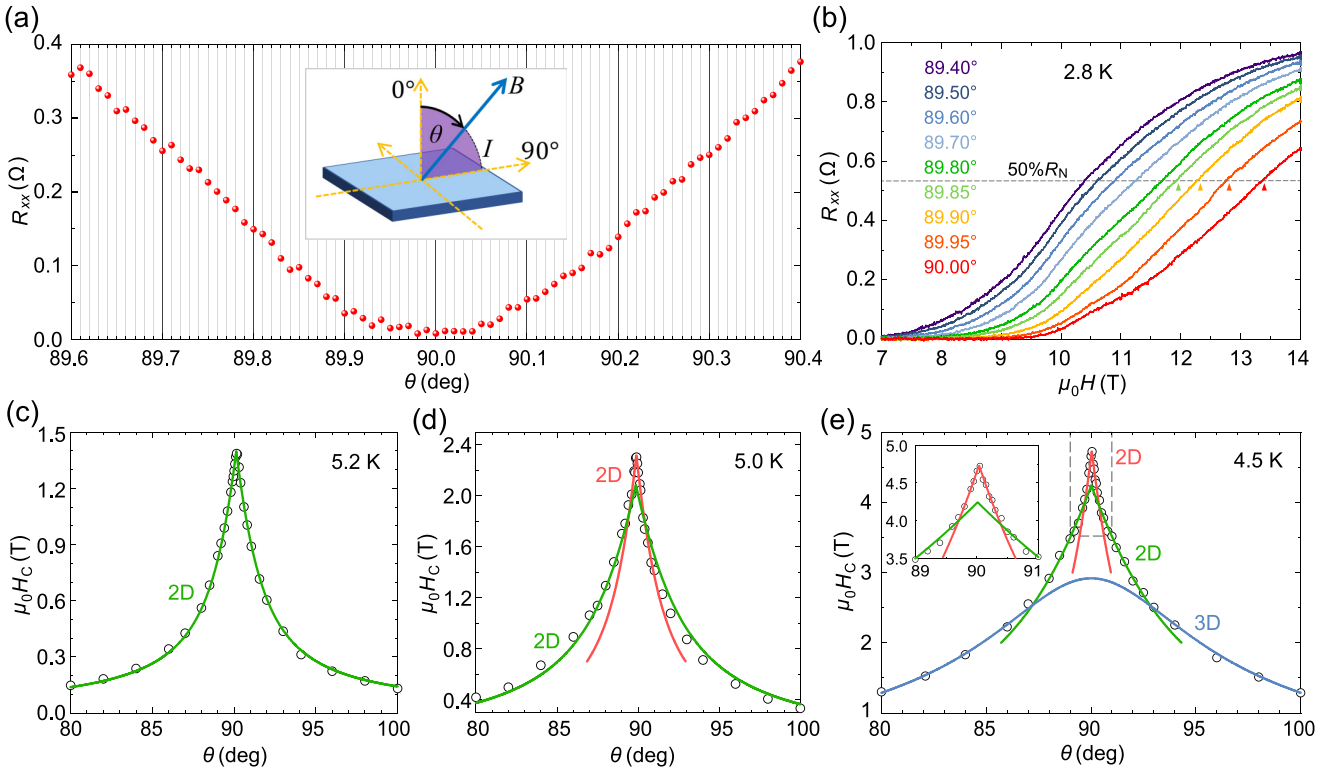


FIG. 2. Confirmation of 2D superconductivity and the analysis of angle-dependent upper critical magnetic field $H_C(\theta)$. (a) $R_{xx}$-$\theta$ relation at $T = 2$ K and $\mu_0 H = 12$ T. An ultrahigh-resolution rotation system can realize measurements with angle resolution down to 0.01°. The inset indicates the definition of $\theta$ in our experiment. (b) The $R_{xx}$-$\mu_0 H$ relation at angles $\theta$ near 90°. The obtained results exhibit excellent signal-to-noise ratios. (c)–(e) Fitting results of $H_C(\theta)$ at 5.2, 5.0, and 4.5 K. All data points, marked by hollow black circles, are derived from the $R_{xx}$-$\mu_0 H$ curves at various angles. Different superconducting components are shown by green (2D), red (sharp-2D), and blue (3D) fitting curves. The fitting results of (c) can directly prove the existence of 2D superconductivity, while the fitting results in (d) imply that there might be two 2D components (named as the 2D and the sharp 2D) existing in the $H_C(\theta)$ measurements. The piecewise function for fitting the $H_C(\theta)$ data in (e) is used based on the following angle ranges: (1) the sharp-2D component fits the data within $90 \pm 0.2°$, (2) the 2D component fits the remaining data in the range of $90 \pm 2°$, and (3) the 3D component fits the remaining data in the range of 0°–180°.

underestimated for multiband superconductors, leading to inappropriate confirmation of the superconductivity dimensionality [27], we do not use this criterion in our study. (2) By determining the shape of $H_C(\theta)$ with $\theta$ near 90° (in-plane applied magnetic field), the $H_C(\theta)$ curve exhibits a cusp peak in the 2D superconducting scenario, while a round-shaped peak is expected in the 3D scenario based on the Ginzburg-Landau theory. The $H_C(\theta)$ expression of an anisotropic 3D superconductor from the Ginzburg-Landau theory [28] can be described by Eq. (1):

$$\left(\frac{H_{C2}(\theta)\sin\theta}{H_{C2,\parallel}}\right)^2 + \left(\frac{H_{C2}(\theta)\cos\theta}{H_{C2,\perp}}\right)^2 = 1. \quad (1)$$

On the other hand, the formula of the $H_C(\theta)$ of 2D superconductors [29] is given by Eq. (2) (Tinkham equation):

$$\left(\frac{H_{C2}(\theta)\sin\theta}{H_{C2,\parallel}}\right)^2 + \left|\frac{H_{C2}(\theta)\cos\theta}{H_{C2,\perp}}\right| = 1. \quad (2)$$

Figure 2(a) shows the $R_{xx}$-$\theta$ relation under magnetic field $\mu_0 H = 12$ T at 2 K, and one can see that our rotator can reach an ultrahigh angle resolution up to 0.01°. Furthermore, Fig. 2(b) shows the $R_{xx}$-$\mu_0 H$ relation at $\theta$ near 90°. Both the above two figures indicate that our sample-rotating measurement system can directly catch the detailed features of the $H_C(\theta)$ relation and the resulting superconducting dimensionality.

As mentioned before, only at the temperature near $T_C = 5.4$ K can we observe the previously discussed deviation from linear extrapolation of the $H_C$-$T$ relation in Fig. 1(d). Therefore, the temperature-dependent $H_C(\theta)$ fitting starts to be critical to understand the dimensionality of the superconducting components and their evolution. We first provide the $H_C(\theta)$ fitting curve at 5.2 K in Fig. 2(c). One can see that Eq. (2) for 2D superconductivity, rather than Eq. (1) for 3D superconductivity, perfectly fits the $H_C(\theta)$ data at 5.2 K, which is expected. Importantly, we notice that the application of a piecewise function can have a better fit for the $H_C(\theta)$ data at 5.0 K [Fig. 2(d)] in the following way: an additional 2D superconducting component (named as "sharp 2D") with a sharper cusp peak (red curve) has to be added in the fitting process besides the above 2D superconducting feature (named as "2D," corresponding to the green curve). While in the $H_C(\theta)$ fitting for 4.5 K [Fig. 2(e)], one more 3D superconducting component (the third component, blue curve) has to be added to fit the data appropriately. Detailed discussions about the

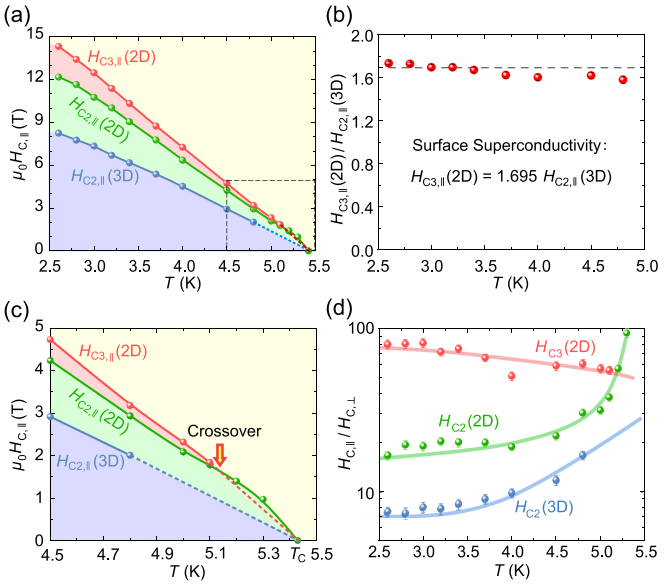


FIG. 3. Distinguishment of 2D and 3D superconductivity based on the analysis of temperature-dependent $H_C(\theta)$. (a) Temperature dependence of $H_{C,\parallel}$ from the three fitted components: the $H_{C3,\parallel}(2D)$ [corresponding to the red curve in Fig. 2(d)], the $H_{C2,\parallel}(2D)$ [corresponding to the green curve in Fig. 2(c)], and the $H_{C2,\parallel}(3D)$ [corresponding to the blue curve in Fig. 2(e)], being marked by red, green, and blue balls, respectively. Note that all the $H_{C,\parallel}$-$T$ curves are extrapolated to the value of $T_C$. (b) The ratio of $H_{C3,\parallel}(2D)$ to $H_{C2,\parallel}(3D)$ as a function of temperature. The values of the ratios are very close to 1.695, implying that the $H_{C3}(2D)$ comes from surface superconductivity of the $H_{C2}(3D)$. (c) Partial enlargement of (a) near $T_C$. A crossover between $H_{C3,\parallel}(2D)$ and $H_{C2,\parallel}(2D)$ can be observed at $T \approx 5.1$ K. (d) Temperature-dependent anisotropy indices $H_{C,\parallel}/H_{C,\perp}$ of the three superconducting components. The trend lines are guides for the eyes. One can see that, as the temperature increases, the anisotropy indices for both $H_{C2}(2D)$ and $H_{C2}(3D)$ increase, while that for the $H_{C3}(2D)$ case decreases.

fitting methods and fitting ranges at different temperatures based on the piecewise function are presented in Figs. S2–S4 [26]. These discussions, combined with the characteristics of the weak subband interactions, prove the rationality of introducing a piecewise function.

Based on the weak interaction assumption for this multiband superconductor [5,16], the cusp peak of $H_C(\theta)$ should be associated with the superconductivity from the 2D subband, while the round peak is related with the superconductivity from the 3D subband. As theoretically confirmed in the band structure of 2H-$NbS_2$, there should be only one 2D-like superconducting subband centered at the $K$ point [16], so the origination of the second 2D superconducting component needs to be further discussed. In order to study the temperature dependence of the above three superconducting components, we systemically analyze $H_C(\theta)$ data at various temperatures from 2.8 to 5.3 K and obtain the following three groups of fitted $H_{C,\parallel}$ values. Similarly, the $H_{C,\perp}$ fitted values can also display a nonlinear $H_{C,\perp}$-$T$ relation, suggesting the existence of multiband superconductivity in 2H-$NbS_2$ (Fig. S5 [26]). As shown in Fig. 3(a), the three groups of $\mu_0 H_{C,\parallel}$ values follow the given relation: sharp 2D (red) > 2D (green) > 3D (blue) at the temperature range from 3 to 5 K. Interestingly, the $H_{C,\parallel}$ ratio of the sharp 2D to the 3D [Fig. 3(b)] is close to the value of 1.695 in a wide temperature range, indicating that this sharp-2D superconducting component originates from the surface superconductivity of the 3D component based on the relation $H_{C3,\parallel}(2D) \approx 1.695 H_{C2,\parallel}(3D)$ in [1]. In general, the surface superconductivity can arise from sample-vacuum and sample-air interfaces, as well as superconductor/insulator heterostructures [1,2]. For a type-II superconductor with such kinds of interfaces, when the applied in-plane magnetic field is larger than $H_{C2}$, the vortex cores inside the bulk overlap with each other and superconductivity is thus extinguished, while superconductivity can still nucleate at the surface of the superconductor and can survive to an even higher field $H_{C3}$ due to the boundary condition which is not imposed in the bulk. Therefore, the surface superconducting component can separate from the bulk components in the following two aspects: (1) For the in-plane critical magnetic field, surface superconductivity can survive at a higher magnetic field than that of the bulk superconductivity. (2) For separation in real space, the surface component is localized only at the surface region in our bulk sample. Both of them make it possible to experimentally confirm the existence of surface superconductivity. Here, we assign the critical field of the 3D component as $H_{C2}(3D)$, and that of the sharp-2D component as $H_{C3}(2D)$. Thus, the critical field of the remaining 2D superconducting component can be defined as $H_{C2}(2D)$, which is strongly related to the 2D-like superconducting subband centered at the $K$ point. Note that the $H_C(\theta)$ relation and the above-mentioned band-dependent dimensionality of superconductivity are highly reproducible in all our measured samples (Fig. S6 [26]), and provide us with the possibility to understand the orbital-selective pairing mechanism in 2H-$NbS_2$.

With further $H_C$-$T$ analysis in the temperature range of 4.5–5.5 K, one can see that the value of $H_{C3,\parallel}(2D)$ starts to be smaller than that of $H_{C2,\parallel}(2D)$ at the temperature above 5.1 K, as displayed in Fig. 3(c). Note that with ignorable interaction between subbands, the $H_C(\theta)$ values obtained from experiments should be equal to the maximum values of the critical field of each superconducting component associated with a certain subband. Therefore, only one 2D component can be experimentally observed at 5.2 K [Fig. 2(c)]. We also plot the anisotropy indices (defined by $H_{C,\parallel}/H_{C,\perp}$) of the three components derived from the fitting results in Fig. 3(d). For the temperature above 5.1 K, the rising tendency of the $H_{C2}(2D)$ component with increasing temperature shows a remarkable difference from that of the sharp-2D component associated with surface superconductivity. This can support our hypothesis that the 2D superconducting component does not come from surface superconductivity but originates from the intrinsic property of thick 2H-$NbS_2$ flakes.

Here, we address that our analysis is always validated and that the above-mentioned phenomena are almost independent of the definition of $H_C$, as presented in Figs. S7–S9 [26]. Specifically, there is a crossover between the $H_{C,\parallel}$ values of the two 2D superconducting components [shown in Fig. 3(c)], and such a crossover remains under different $H_C$ definitions. The above experiments and analysis further confirm that the sharp-2D component associated with $H_{C3}(2D)$

comes from the surface superconductivity of thick flakes with the 3D component $H_{C2}(3D)$, and that the other 2D component $H_{C2}(2D)$, together with $H_{C2}(3D)$, might be intrinsic superconducting properties of bulk 2H-$NbS_2$ with orbital-selective multiband nature, originating from the superconducting gaps centered at the $K$ and $\Gamma$ points, respectively. The previous study on the $H_C(\theta)$ of the bulk 2H-$NbS_2$ crystal could only show evidence of one 3D component with a round peak [30], probably because the misalignment of mosaic microstructures in the large-size sample broadens the cusp peak in the $H_C(\theta)$ curve. It should be addressed that the Fulde-Ferrell-Larkin-Ovchinnikov (FFLO) state [31,32] can also exhibit an anomalous cusp-peak behavior of $H_C(\theta)$, which has been discussed in two recent reports [33,34]. However, note that the FFLO state typically exists only in an extremely low temperature range [35], so the fact that the cusp peak in our observation remains at temperatures up to 5.2 K [over 95% $T_C$ in Fig. 2(c)] excludes the contribution from the FFLO state in such a multiband superconductor.

As shown by the green curve in the inset of Fig. 2(e), the $H_{C2,\parallel}(2D)$ value cannot be determined directly from the experimental observation of $H_C(\theta)$ due to the larger $H_{C3}(2D)$ value within the regime of $\theta = 90 \pm 0.2^\circ$. Therefore, we design controlled experiments to suppress the surface superconductivity and to further confirm the existence of the intrinsic 2D superconducting component of 2H-$NbS_2$. Here, we use the following three methods to suppress the surface superconductivity and the resulting $H_{C3}$, including applying a large electric current [36], utilizing a high-pressure technique [37], or inducing an antiproximity effect [1,2] by depositing gold film on the 2H-$NbS_2$ surface. Correspondingly, we investigate the multiband superconducting behavior of 2H-$NbS_2$ with the $H_C(\theta)$ measurements for the above three situations, as shown in Fig. 4 and Fig. S10 [26]. The particular sample we use for the large current measurement shows a critical temperature $T_C = 5.7$ K with the applied electric current $I = 250$ $\mu$A, which is very close to the value of the critical superconducting current [Figs. 4(a), 4(b), and Fig. S11 [26]]. The intrinsic superconducting properties remain the same as those in the previous measurements with small electric current, while the extrinsic surface superconductivity is expected to be effectively suppressed by the large current [36]. The fitting results in Fig. 4(a) apparently contain only one 2D component associated with $H_{C2}(2D)$ for $T = 4.5$ K, while the $H_{C3}(2D)$ component originating from surface superconductivity is observed at a lower temperature $T = 4.25$ K shown in Fig. 4(b), which is in sharp contrast with the $H_{C3}(2D)$ observed at a higher temperature of 5.0 K [Fig. 2(d)]. Note that the observable temperature of surface superconductivity shown as the crossover point in Fig. 4(b) (78% $T_C$) is much lower than that in Fig. 3(c) (94% $T_C$). Thus, the surface superconductivity is significantly suppressed since the large current density exceeds its critical current value, similar to the previous report on current-induced suppression of surface superconductivity [36].

Since a high-pressure technique can effectively suppress surface superconductivity [37] while maintaining the multiband nature of the superconducting 2H-$NbS_2$ system [20], we perform the $H_C(\theta)$ measurement with a diamond anvil cell high-pressure technique and investigate

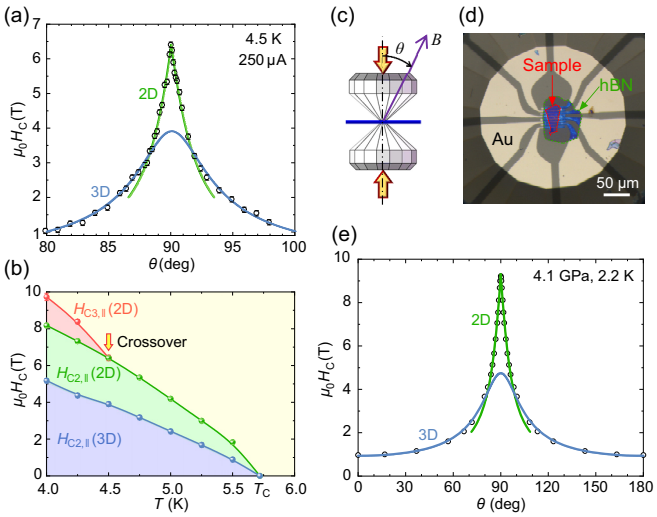


FIG. 4. Investigation of intrinsic 2D superconductivity by applying large electrical current (a), (b) and high pressure (c)–(e). (a) The $H_C(\theta)$ fitting results with a large electric current intentionally chosen as $I = 250$ $\mu$A for 4.5 K. (b) Temperature-dependent $H_{C,\parallel}$ from the three fitted components, $H_{C3,\parallel}(2D)$, $H_{C2,\parallel}(2D)$, and $H_{C2,\parallel}(3D)$. These values, marked by red, green, and blue balls, are smoothly connected by $B$-spline curves. The crossover temperature decreases compared with Fig. 3(c), indicating that surface superconductivity is apparently suppressed, but the $H_{C2}(2D)$ is still able to maintain in the large current condition. (c) A cartoon picture for high-pressure measurement geometry. (d) An optical photograph of the device. The sample (red dashed line) is covered by hexagonal BN (hBN) film (green dashed line). (e) The $H_C(\theta)$ relation and fitting results under 4.1 GPa. The data points among 90°–180° are obtained at 2.2 K by symmetrizing the 0°–90° data after reaching the maximum magnetic field. A single 2D superconducting component (green line) shows good fitting results with Eq. (2) near $H \parallel ab$.

the band-dependent dimensionality and orbital-selective superconductivity in multiband 2H-$NbS_2$. Figures 4(c) and 4(d) present the schematic illustration and optical image of the device. As shown in Fig. 4(e), the surface superconducting component associated with $H_{C3}$ is effectively suppressed under 4.1 GPa at 2.2 K, while the other two superconducting components still exist in our $H_C(\theta)$ fitting results. The ratio $H_{C,\parallel}(2D)/H_{C2,\parallel}(3D) = 9.33/4.74 \approx 1.97$ is significantly larger than 1.695 [Fig. 3(b)], implying that the observed 2D component under high pressure is associated with the $H_{C2}(2D)$ rather than the $H_{C3}(2D)$. Generally speaking, unlike the superconductivity associated with the $H_{C3}(2D)$, the superconductivity correlated with $H_{C2}(2D)$ seems to be more robust and cannot be eliminated either by applying a large current or under high pressure. Therefore, we confirm the superconducting component associated with $H_{C2}(2D)$ as the intrinsic superconductivity behavior of 2H-$NbS_2$. More details of high-pressure $H_C(\theta)$ analysis are given in Fig. S12 [26].

## III. DISCUSSION

The intrinsic $H_{C2}(2D)$ superconducting component might come from the strongly anisotropic subband centered at the $K$ point. According to previous reports on theoretical

calculation [16] and angle-resolved photoemission spectroscopy [38], together with our *ab initio* calculations, intrinsic bulk 2H-$NbS_2$ is a metal with three distinct Fermi surface sheets [lower panel of Fig. 1(a)]. The hole pockets centered at the Γ point (marked by $S_{\Gamma 1}$ and $S_{\Gamma 2}$, respectively) are mainly contributed by the out-of-plane $p_z$ orbital of S atoms and $d_{z^2}$ orbital of Nb atoms. The third anisotropic triangular hole pocket centered at the $K$ point (marked by $S_K$) is mainly contributed by the in-plane $d_{xy}$ and $d_{x^2-y^2}$ orbitals of Nb atoms. These Fermi surface sheets are fully gapped via pairing mediated by electron-phonon interactions, making 2H-$NbS_2$ an orbital-selective two-gap Bardeen-Cooper-Schrieffer (BCS) superconductor [16]. The smaller gap is associated with Fermi surface sheets $S_{\Gamma 1}$ and $S_{\Gamma 2}$, while the larger one belongs to $S_K$. In sharp contrast to the BCS pairing on the Fermi surface sheets $S_{\Gamma 1}$ and $S_{\Gamma 2}$, the hole pocket $S_K$ couples with itself by two anharmonic phonon modes along the Γ-$M$ direction, forming the Cooper pairs and exhibiting a highly anisotropic superconducting character. Such reported results [16] strongly support our expectation of distinguishing two intrinsic pairing mechanisms in this orbital-selective multiband superconductor. Therefore, we believe that the 3D subband associated with $H_{C2}$(3D) might come from the pairing within $S_{\Gamma 1}$ and $S_{\Gamma 2}$ sheets, while the intrinsic 2D subband associated with $H_{C2}$(2D) might originate from the strongly anisotropic superconducting pairing in the $S_K$ sheet.

Such understandings of the superconducting dimensionalities based on the $k$-space Fermi surface distribution can be further extended to the Josephson coupling between superconducting layers in real space. For the case of 2H-$NbS_2$, since the interaction between the two superconducting subbands seems very weak, the effect for the two subbands should be discussed individually: (1) For the intrinsic 3D superconducting subband, the Josephson coupling can be large to some extent, leading to the feature of anisotropic 3D superconductivity. (2) For the intrinsic 2D superconducting subband, however, since the dispersion along the out-of-plane direction is absent, the Josephson coupling effect becomes extremely weak. As a result, orbital-selective 2D superconductivity appears even though the superconducting $NbS_2$ layers are in direct contact.

Combining the above-mentioned discussions on 2H-$NbS_2$ with the calculation and experimental works on 2H-$NbSe_2$ [7,14], we address that such an orbital-selective 2D superconductivity is also supposed to exist in the counterpart material, 2H-$NbSe_2$. However, considering the small anisotropy index in this system [25], together with the possible interaction between superconductivity and the charge density wave phase [17,22,23], the direct experimental confirmation might be impeded. Our results show that the pristine 2H-$NbS_2$ sample already hosts 2D superconductivity without introducing insulating layers to artificially separate atomically thin superconducting layers. Such understandings of the band-dependent dimensionalities and orbital-selective pairing mechanism of 2H-$NbS_2$ help us better understand the effect of insulating layers between superconducting layers in artificial superlattices [33], and can also be extended to other multiband superconductors, such as FeSe and $MgB_2$ [3,39].

## IV. CONCLUSION

In summary, based on the comprehensive analysis of $H_C(\theta)$, we experimentally demonstrate the intrinsic orbital-selective 2D superconductivity originating from the strongly anisotropic 2D superconducting subband from the $d$ orbitals of Nb atoms in thick 2H-$NbS_2$ flakes. Our analysis of $H_C(\theta)$ can be more generally applied to other multiband superconductors to achieve a better understanding of band-dependent dimensionalities of superconductivity. Thus, unlike the reported 2D superconductivity with Cooper pairs confined in nanostructures with limited thickness, such as monolayers [6,10,40,41], interfaces [42–44], and superlattices [33,45,46], our results can provide a bulk material platform for 2D superconductivity based on an orbital-selective pairing mechanism in multiband superconductors.

## ACKNOWLEDGMENTS

This work was supported by the A3 Foresight Program—Emerging Materials Innovation. The authors would like to acknowledge the support by the National Natural Science Foundation of China (Grants No. 51861145201, No. 91750101, No. 21733001, and No. 52072168), the National Key Basic Research Program of the Ministry of Science and Technology of China (2018YFA0306200), and the Fundamental Research Funds for the Central Universities (Grants No. 021314380078, No. 021314380104, and No. 021314380147). T.I. and Y.I. would also like to acknowledge the A3 Foresight program and KAKENHI Grant No. JP19H05602 from the Japan Society for the Promotion of Science (JSPS). T.N. was supported by JSPS KAKENHI Grant No. JP21H01792. The calculations were supported by the high-performance computing (HPC) resources at Beihang University.

X.Y.B., Z.Y.L., and J.W.H. contributed equally to this work. H.T.Y. and Y.I. conceived the project and designed the experiments. X.Y.B., Z.Y.L., F.Q., and M.T. prepared devices, and C.R.Z. and L.Z. performed high-pressure measurements. X.Y.B., Z.Y.L., F.Q., and J.W.H. carried out electronic transport measurements. Z.A.X. and P.Z.T. carried out the first-principles calculations. X.Y.B., C.Y.Q., P.Z.T., T.I., and T.N. discussed and analyzed the experimental data. X.Y.B., F.Q., and H.T.Y. wrote the manuscript with input from all authors.

## APPENDIX: MATERIALS AND METHODS

### 1. Device fabrication

Bulk-form 2H-$NbS_2$ crystal is obtained by a chemical vapor transmission method. The precursors are mixed with a Nb:S ratio of 1:2.07, and the mixture is heated at 1050 °C with a ramping rate of 0.8 °C/min, and the temperature is held constant for 7 days for reaction. Then, the furnace is cooled to 850 °C with a ramping rate of 0.2 °C/min, and is kept at this temperature for 1 day for annealing. Finally, the product is quenched to room temperature by placing it into water. 2H-$NbS_2$ flakes are obtained by mechanically exfoliating the as-prepared bulk crystal in an $N_2$ glovebox and transferred on $Si/SiO_2$ substrates with polydimethylsiloxane (PDMS) film. The polymethyl methacrylate (PMMA) is then spin-coated on

the substrate and heated at 180 °C for 1.5 min. A standard electron beam lithography process is used for device fabrication, and 6/50-nm-thick Ti/Au electrodes are evaporated. The devices are finally spin-coated by PMMA to avoid air exposure. The thickness of all measured samples ranges from 35 to 45 nm and is confirmed by atomic force microscopy after transport measurements.

### 2. Low-temperature electronic transport

The electronic transport properties of the devices are measured in Oxford Instruments Teslatron and in a Quantum Design physical property measurement system. Both the four-terminal resistance $R_{xx}$ and the Hall resistance $R_{xy}$ are obtained using an SR830 (Stanford Research Systems) lock-in amplifier by AC method with frequency $f = 13$ Hz. A homemade ultrahigh-resolution sample rotator, whose stepping motor can reach an accuracy limit up to 0.01°, is applied for characterizing the angular distribution of upper critical magnetic field $H_C(\theta)$. The pressure-dependent electronic transport experiments are performed in a screw-pressure-type diamond anvil cell. The pressure is calibrated using the fluorescence shift of ruby balls at room temperature.

### 3. The first-principles calculations

The first-principles density functional theory (DFT) calculations are performed by using the projector-augmented wave method [47,48] implemented in the Vienna *ab initio* Simulation Package (VASP) [49]. The energy cutoff for the plane wave basis is set to be 600 eV. We use the exchange correlation functional of generalized gradient approximation with Perdew-Burke-Ernzerhof type to relax the lattice and calculate the electronic structures, and the van der Waals correction with the DFT-D2 method [50] is also included to describe the interlayer coupling correctly. For the self-consistent electronic structure calculations, we set the energy convergence criterion as $10^{-6}$ eV and the $k$-point mesh as $24 \times 24 \times 8$ over the whole Brillouin zone.


[1] M. Tinkham, *Introduction to Superconductivity* (Courier Corporation, North Chelmsford, MA, 2004).

[2] V. V. Schmidt, *The Physics of Superconductors: Introduction to Fundamentals and Applications*, edited by P. Muller and A. V. Ustinov (Springer Science & Business Media, New York, 1997).

[3] P. O. Sprau, A. Kostin, A. Kreisel, A. E. Böhmer, V. Taufour, P. C. Canfield, S. Mukherjee, P. J. Hirschfeld, B. M. Andersen, and J. C. S. Davis, Discovery of orbital-selective Cooper pairing in FeSe, Science **357**, 75 (2017).

[4] J. Nagamatsu, N. Nakagawa, T. Muranaka, Y. Zenitani, and J. Akimitsu, Superconductivity at 39 K in magnesium diboride, Nature (London) **410**, 63 (2001).

[5] Q. Li, B. T. Liu, Y. F. Hu, J. Chen, H. Gao, L. Shan, H. H. Wen, A. V. Pogrebnyakov, J. M. Redwing, and X. X. Xi, Large Anisotropic Normal-State Magnetoresistance in Clean $MgB_2$ Thin Films, Phys. Rev. Lett. **96**, 167003 (2006).

[6] X. Xi, Z. Wang, W. Zhao, J.-H. Park, K. T. Law, H. Berger, L. Forró, J. Shan, and K. F. Mak, Ising pairing in superconducting $NbSe_2$ atomic layers, Nat. Phys. **12**, 139 (2016).

[7] T. Yokoya, T. Kiss, A. Chainani, S. Shin, M. Nohara, and H. Takagi, Fermi surface sheet-dependent superconductivity in 2H-$NbSe_2$, Science **294**, 2518 (2001).

[8] B. Sipos, A. F. Kusmartseva, A. Akrap, H. Berger, L. Forró, and E. Tutiš, From Mott state to superconductivity in 1T-$TaS_2$, Nat. Mater. **7**, 960 (2008).

[9] M. Hashimoto, I. M. Vishik, R. H. He, T. P. Devereaux, and Z. X. Shen, Energy gaps in high-transition-temperature cuprate superconductors, Nat. Phys. **10**, 483 (2014).

[10] L. J. Li, E. C. T. O'Farrell, K. P. Loh, G. Eda, B. Özyilmaz, and A. H. C. Neto, Controlling many-body states by the electric-field effect in a two-dimensional material, Nature (London) **529**, 185 (2016).

[11] L. Jiao, S. Howard, S. Ran, Z. Wang, J. O. Rodriguez, M. Sigrist, Z. Wang, N. P. Butch, and V. Madhavan, Chiral superconductivity in heavy-fermion metal $UTe_2$, Nature (London) **579**, 523 (2020).

[12] Y. Cao, J. M. Park, K. Watanabe, T. Taniguchi, and P. Jarillo-Herrero, Pauli-limit violation and re-entrant superconductivity in moiré graphene, Nature (London) **595**, 526 (2021).

[13] J. M. Park, Y. Cao, K. Watanabe, T. Taniguchi, and P. Jarillo-Herrero, Tunable strongly coupled superconductivity in magic-angle twisted trilayer graphene, Nature (London) **590**, 249 (2021).

[14] M. D. Johannes, I. I. Mazin, and C. A. Howells, Fermi-surface nesting and the origin of the charge-density wave in $NbSe_2$, Phys. Rev. B **73**, 205102 (2006).

[15] S. V. Borisenko, A. A. Kordyuk, V. B. Zabolotnyy, D. S. Inosov, D. Evtushinsky, B. Büchner, A. N. Yaresko, A. Varykhalov, R. Follath, W. Eberhardt, L. Patthey, and H. Berger, Two Energy Gaps and Fermi-Surface "Arcs" in $NbSe_2$, Phys. Rev. Lett. **102**, 166402 (2009).

[16] C. Heil, S. Poncé, H. Lambert, M. Schlipf, E. R. Margine, and F. Giustino, Origin of Superconductivity and Latent Charge Density Wave in $NbS_2$, Phys. Rev. Lett. **119**, 087003 (2017).

[17] K. Rossnagel, E. Rotenberg, H. Koh, N. V. Smith, and L. Kipp, Fermi surface, charge-density-wave gap, and kinks in 2$H$-$TaSe_2$, Phys. Rev. B **72**, 121103 (2005).

[18] I. Guillamón, H. Suderow, S. Vieira, L. Cario, P. Diener, and P. Rodière, Superconducting Density of States and Vortex Cores of 2H-$NbS_2$, Phys. Rev. Lett. **101**, 166407 (2008).

[19] J. Kačmarčík, Z. Pribulová, C. Marcenat, T. Klein, P. Rodière, L. Cario, and P. Samuely, Specific heat measurements of a superconducting $NbS_2$ single crystal in an external magnetic field: Energy gap structure, Phys. Rev. B **82**, 014518 (2010).

[20] V. G. Tissen, M. R. Osorio, J.-P. Brison, N. M. Nemes, M. Garcia-Hernandez, L. Cario, P. Rodière, S. Vieira, and H. Suderow, Pressure dependence of superconducting critical temperature and upper critical field of 2$H$-$NbS_2$, Phys. Rev. B **87**, 134502 (2013).

[21] H. Huang, Y. Lu, and X. Huang, Two-band analysis on the upper critical field for superconductor $NbS_2$, Eur. Phys. J. B **86**, 135 (2013).

[22] X. Xi, L. Zhao, Z. Wang, H. Berger, L. Forró, J. Shan, and K. F. Mak, Strongly enhanced charge-density-wave order in monolayer $NbSe_2$, Nat. Nanotechnol. **10**, 765 (2015).

[23] D. Lin *et al.*, Patterns and driving forces of dimensionality-dependent charge density waves in 2*H*-type transition metal dichalcogenides, Nat. Commun. **11**, 2406 (2020).

[24] M. Leroux, M. Le Tacon, M. Calandra, L. Cario, M.-A. Measson, P. Diener, E. Borrissenko, A. Bosak, and P. Rodière, Anharmonic suppression of charge density waves in 2*H*-$NbS_2$, Phys. Rev. B **86**, 155125 (2012).

[25] S. Foner and E. J. McNiff, Jr., Upper critical fields of layered superconducting $NbSe_2$ at low temperature, Phys. Lett. A **45**, 429 (1973).

[26] See Supplemental Material at http://link.aps.org/supplemental/10.1103/PhysRevResearch.4.013188 for the sample thickness, fitting methods, multiband analysis on $H_{C,\perp}$, data reproducibility, and fitting for different $H_C$ definitions, results for Au-coated devices, temperature-dependent critical current, as well as fitting results at 3.2 GPa.

[27] T. Klein, L. Lyard, J. Marcus, Z. Holanova, and C. Marcenat, Magnetic field dependence of the coherence length and penetration depth of $MgB_2$ single crystals, Phys. Rev. B **73**, 184513 (2006).

[28] R. C. Morris, R. V. Coleman, and R. Bhandari, Superconductivity and magnetoresistance in $NbSe_2$, Phys. Rev. B **5**, 895 (1972).

[29] M. Tinkham, Effect of fluxoid quantization on transitions of superconducting films, Phys. Rev. **129**, 2413 (1963).

[30] K. Onabe, M. Naito, and S. Tanaka, Anisotropy of upper critical field in superconducting 2*H*-$NbS_2$, J. Phys. Soc. Jpn. **45**, 50 (1978).

[31] P. Fulde and R. A. Ferrell, Superconductivity in a Strong Spin-Exchange Field, Phys. Rev. **135**, A550 (1964).

[32] A. I. Larkin and Y. N. Ovchinnikov, Nonuniform state of superconductors, Sov. Phys. JETP **20**, 762 (1965).

[33] A. Devarakonda, H. Inoue, S. Fang, C. Ozsoy-Keskinbora, T. Suzuki, M. Kriener, L. Fu, E. Kaxiras, D. C. Bell, and J. G. Checkelsky, Clean 2D superconductivity in a bulk van der Waals superlattice, Science **370**, 231 (2020).

[34] C.-w. Cho, J. Lyu, C. Y. Ng, J. J. He, K. T. Lo, D. Chareev, T. A. Abdel-Baset, M. Abdel-Hafiez, and R. Lortz, Evidence for the Fulde–Ferrell–Larkin–Ovchinnikov state in bulk $NbS_2$, Nat. Commun. **12**, 3676 (2021).

[35] W. A. Coniglio, L. E. Winter, K. Cho, C. C. Agosta, B. Fravel, and L. K. Montgomery, Superconducting phase diagram and FFLO signature in λ-$(BETS)_2GaCl_4$ from rf penetration depth measurements, Phys. Rev. B **83**, 224507 (2011).

[36] L. Lyard *et al.*, Anisotropy of the upper critical field and critical current in single crystal $MgB_2$, Phys. Rev. B **66**, 180502 (2002).

[37] S. Gabáni *et al.*, High-pressure effect on the superconductivity of $YB_6$, Phys. Rev. B **90**, 045136 (2014).

[38] Z. El Youbi, S. W. Jung, C. Richter, K. Hricovini, C. Cacho, and M. D. Watson, Fermiology and electron-phonon coupling in the 2*H* and 3*R* polytypes of $NbS_2$, Phys. Rev. B **103**, 155105 (2021).

[39] S. Tsuda, T. Yokoya, S. Shin, Y. Takano, H. Kito, A. Matsushita, F. Yin, J. Itoh, and H. Harima, The Fermi surface and sheet-dependent superconducting gap of $MgB_2$, Physica C **412-414**, 36 (2004).

[40] Y. Cao, V. Fatemi, S. Fang, K. Watanabe, T. Taniguchi, E. Kaxiras, and P. Jarillo-Herrero, Unconventional superconductivity in magic-angle graphene superlattices, Nature (London) **556**, 43 (2018).

[41] E. Sajadi, T. Palomaki, Z. Fei, W. Zhao, P. Bement, C. Olsen, S. Luescher, X. Xu, J. A. Folk, and D. H. Cobden, Gate-induced superconductivity in a monolayer topological insulator, Science **362**, 922 (2018).

[42] J. T. Ye, Y. J. Zhang, R. Akashi, M. S. Bahramy, R. Arita, and Y. Iwasa, Superconducting dome in a gate-tuned band insulator, Science **338**, 1193 (2012).

[43] N. Reyren *et al.*, Superconducting interfaces between insulating oxides, Science **317**, 1196 (2007).

[44] Y. Saito, Y. Kasahara, J. Ye, Y. Iwasa, and T. Nojima, Metallic ground state in an ion-gated two-dimensional superconductor, Science **350**, 409 (2015).

[45] M. H. Hamidian *et al.*, Detection of a Cooper-pair density wave in $Bi_2Sr_2CaCu_2O_{8+x}$, Nature (London) **532**, 343 (2016).

[46] I. Božović, X. He, J. Wu, and A. T. Bollinger, Dependence of the critical temperature in overdoped copper oxides on superfluid density, Nature (London) **536**, 309 (2016).

[47] P. E. Blöchl, Projector augmented-wave method, Phys. Rev. B **50**, 17953 (1994).

[48] G. Kresse and D. Joubert, From ultrasoft pseudopotentials to the projector augmented-wave method, Phys. Rev. B **59**, 1758 (1999).

[49] G. Kresse and J. Hafner, *Ab initio* molecular dynamics for liquid metals, Phys. Rev. B **47**, 558 (1993).

[50] S. Grimme, Semiempirical GGA-type density functional constructed with a long-range dispersion correction, J. Comput. Chem. **27**, 1787 (2006).